Chapter 5

Detector Performances

5.1 Calorimetric features

A Geant3 [1] based Monte Carlo program has been used to study the calorimetric features of the proposed setup. The simulation of the detector response is given with high accuracy, describing the granularity of the module up to the 2 mm fiber and introducing a low energy cut for radiative processes ($E_{th} = 300$ keV), connected to the particle propagation into the medium.

The detector simulation is done considering:

- Statistical Poisson fluctuations of the number of primary photo-electrons (p.e.). According to the measured light yield for a minimum ionizing particle (m.i.p.), a mean value of 20 p.e./MeV on each PMT is assumed (see Chapter 4).
- The light produced by the passage of the particles is propagated along the fibers introducing gaussian fluctuations of about 15% around the estimated attenuation length (5 m).
- The gain of PMT's is assumed equal to to $1.5 \cdot 10^7$, with allowed fluctuations of the order of 30%, to take into account both quantum conversion efficiency fluctuations and Poisson fluctuations in the number of secondary electrons extracted.
- The charge threshold on PMT's is set at about 4 p.e. corresponding to the minimum light yield for a m.i.p. crossing a BCE.

In order to explore the calorimetric features of our apparatus, several samples of muons, electrons and pions, at fixed angles ($\varphi = 0^o, \vartheta = 90^o$) and

with energy in the range $0.3 \div 6\ GeV$, were generated in the first layers of the calorimeter.

Several possible trigger conditions, based only on the calorimeter response, have been simulated. A trigger defined by at least three adjacent fired BCE provides a good detection efficiency for single particles, as shown in Fig. 5.1, with a negligible background contribution. The energy threshold, defined at the 50% of detection efficiency, is about 300-400 MeV. In the hypothesis of the use of RPC's as tracking detectors it is possible to lower the energy threshold using the RPC's also in the trigger. The request of a coincidence between 1 BCE and the 2 adjacent RPC's allows to obtain a lower energy trigger with a background rate compatible with the data acquisition system (see section 3.3.1).

In Fig. 5.2 is shown the charge produced by a muon crossing a BCE; if compared to that relative to the test results (Fig. 4.7), a reasonable agreement is found between simulations and data, also considering that the simulated distribution only concerns horizontal muons.

In the proposed calorimeter the volume ratio between iron ore absorber, as passive material, and fibers, as active material, is 15:1. The visible energy released by the cascades induced by electrons and pions as a function of the incident energy is shown in Fig. 5.3. It is possible to estimate for an electron that the 1.7% of its energy will be measured by our calorimeter, with very good linearity. The response to hadronic showers, very similar to that relative to the electron ones, makes us confident to obtain energy compensation.

The simulated energy resolutions, in Fig. 5.4, are respectively

$$\sigma(E)/E = 0.01 + 0.17/\sqrt{E}$$

for electromagnetic and

$$\sigma(E)/E = 0.08 + 0.42/\sqrt{E}$$

for hadronic showers, where E is in Gev. Taking into account the total mass of the calorimeter and the resulting limited sampling these figures are rather good.

The penetration of electrons, muons and pions in the calorimeter are shown in Fig. 5.5 as a function of energy. Note that a muon crosses more than 10 layers of BCE per GeV.

Many energy measurements along the particle track will be used to measure with high accuracy the specific ionization of a m.i.p. allowing for its separation from showering particles. Furthermore, it is straightforward to

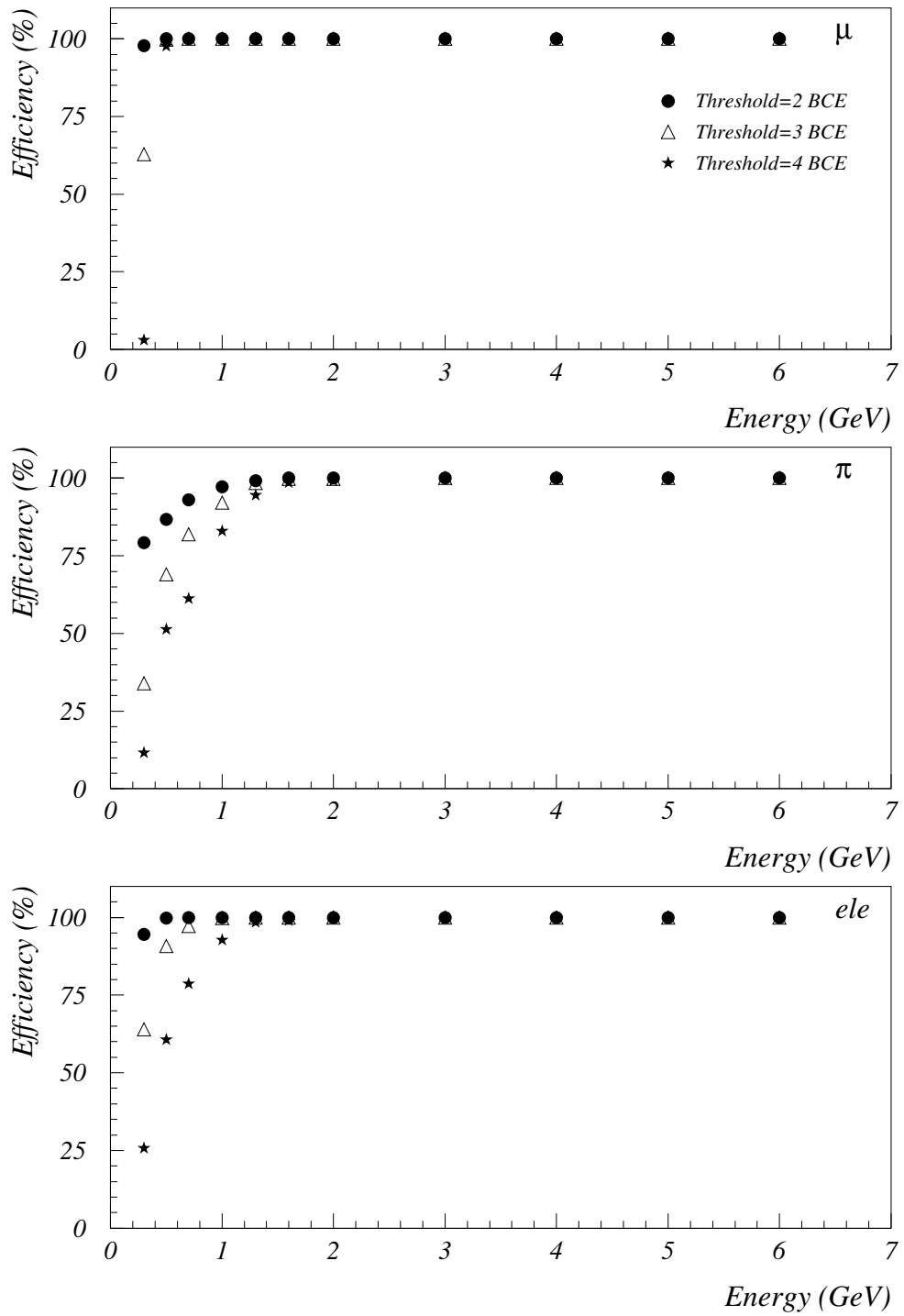

Figure 5.1: Detection efficiency for single particles as a function of the incident energy.

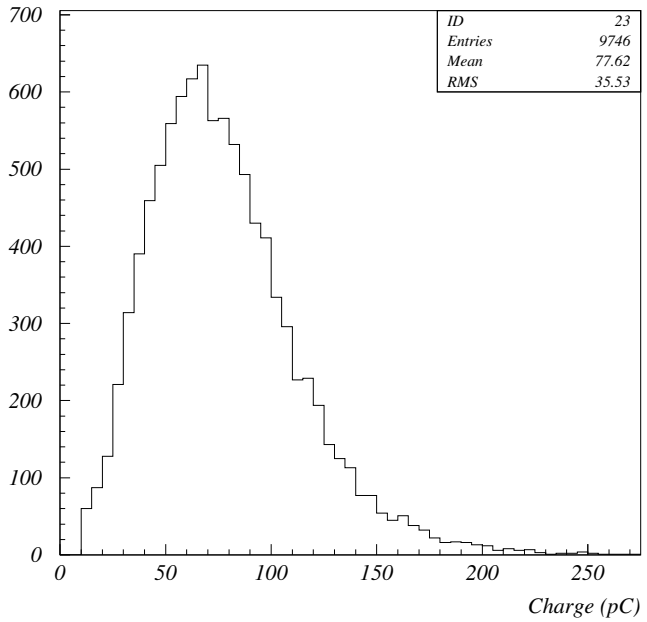

Figure 5.2: The simulated charge distribution for a muon crossing a BCE.

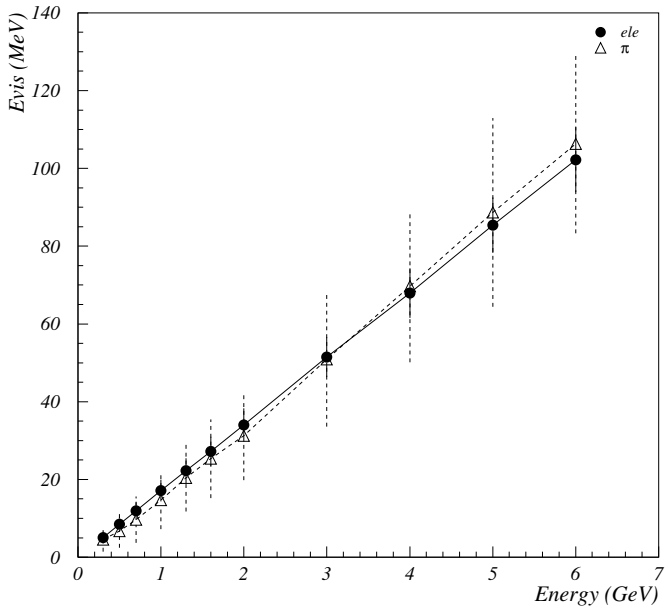

Figure 5.3: The visible energy released by the cascades induced by electrons or pions as a function of E_o. The lines are drawn to guide the eye.

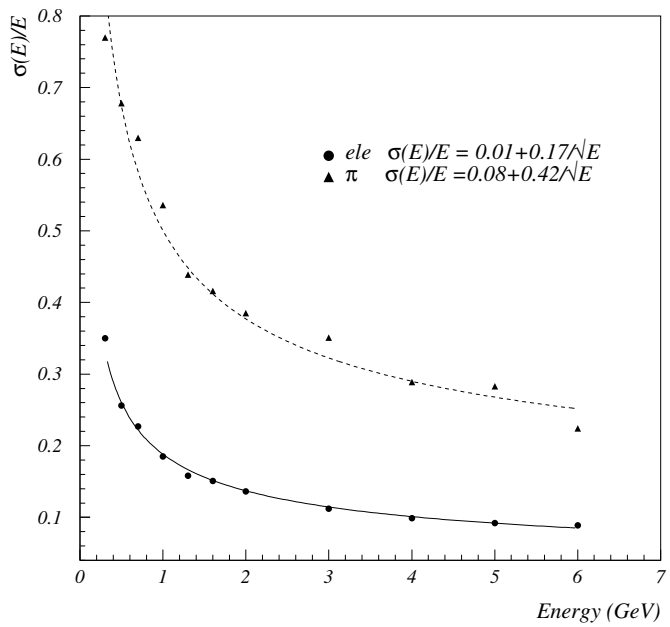

Figure 5.4: Simulated energy resolutions for electromagnetic and hadronic showers.

calculate that the complete N^OE detector (see section 3.1.2) will be able to stop horizontal muons up to 20 GeV ($R_\mu \geq 10\ layers/GeV$).

It is also evident, from Fig. 5.5 and from the shower profile (see Fig. 5.10), that no more than 12-14 planes are needed to contain longitudinally showers up to 6 GeV. This represents a good feature to separate CC from NC produced events.

From these first results such a kind of scintillating fiber calorimeter seems to be a good choice for energy measurement due to its large stopping power, good energy resolution and the possibility to obtain almost equal signals for electrons and hadrons of the same energy.

5.2 Tracking performances

In order to study the performances of the tracking system, the simulation of the streamer tube (see Sect. 3.2) has been inserted in our Monte Carlo. A preliminary tracking algorithm has been implemented, working mainly on long tracks. Therefore it has been possible to check the angular resolution of the detector made with 2 cm streamer elements. In Figures 5.6 the resolution

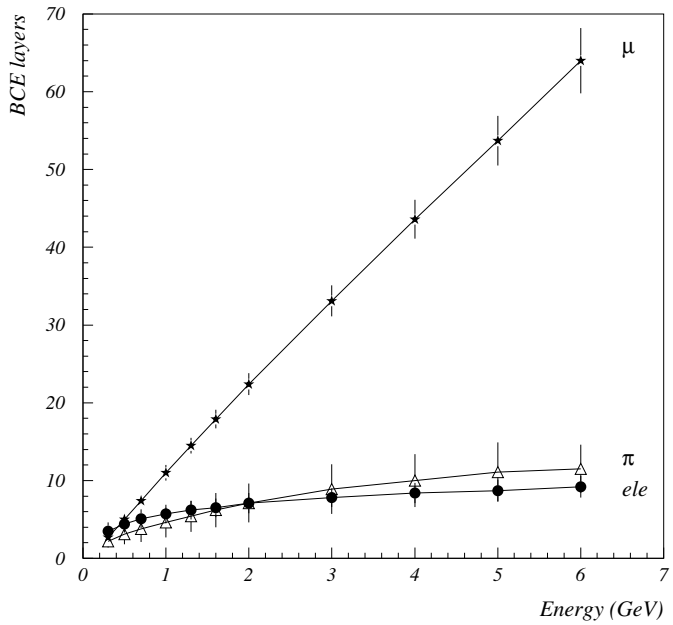

Figure 5.5: Layers of BCE crossed by different particles as a function of the incident energy.

is shown for different ν beams and μ energies. The results of this simulation should be similar in the case of resistive plate counters as tracking system.

The informations deduced by means of tracking analysis will be employed to measure the range and the transverse momentum of each particle and its path lengths Δl in the BCE elements. In this way the value of $\frac{\Delta E}{\Delta l}$ (see section 5.3) can be determined with higher accuracy. Furthermore the check of coplanarity of ν beam, μ track and shower axis is a way to look for ν_τ charged current (see Sect. 6.3.2).

Another possibility still under investigation is to use the multiple scattering estimation as a check of the measured energy of the particle.

The calorimeter elements can also be used for tracking purposes, in particular to reconstruct the shower axis direction. In fact it is possible to get shower center of mass in each calorimetric plane by means of energy weights. In the present design, the calorimetric elements are piled up on the top of each other making simpler the mechanical structure. The shower axis is obtained combining the center of gravity of the energy deposited in each calorimetric plane (X_E) and two (X_{hits}, Y_{hits}) hit cluster centers in each plane of tracker. In a different approach the fiber planes are crossed alternatively in horizon-

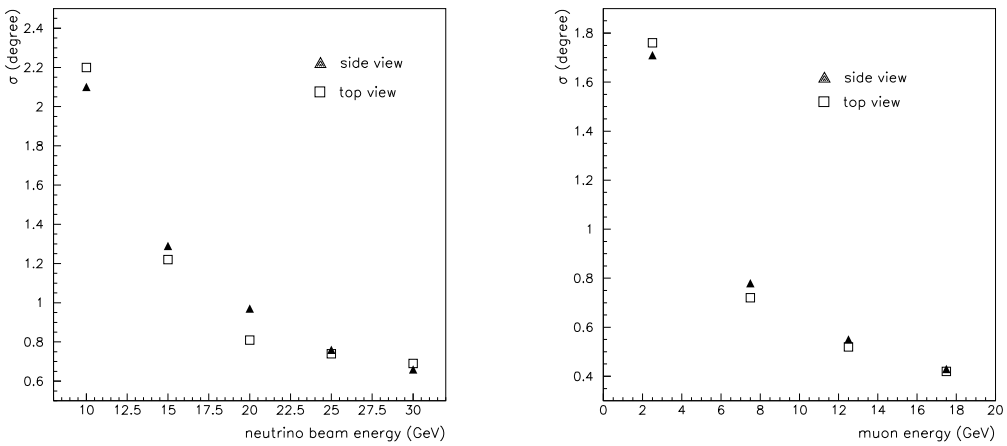

Figure 5.6: Angular resolution of the muon direction in two projected planes (side and top views). The muons are generated in charged current interactions of beam ν's inside the detector. Five different beam energies have been used (see first figure). In the second figure the resolution is displayed as a function of the μ energy (each point represents the mean value in a 5 GeV range).

tal and vertical directions. From the mechanical point of view, this layout is more difficult, but it should improve the shower direction measurement, allowing to combine two center of gravity of the energy deposit (X_E, Y_E) and two (X_{hits}, Y_{hits}) hit cluster centers.

The final layout choice will depend on comparison of construction difficulty and resolution power in the shower direction measurement.

5.3 Particle identification

Particle identification is in general obtained by the measurement of any two physics variables which are related via the mass. Many possibilities are available, in our case we use the measurement of $\left(\frac{dE}{dx}\right)$ and energy E.

The capability of the experiment to measure energy loss (ΔE) and the path (Δl) in each basic calorimetric element, many times along the track, allows particle identification using the $\frac{\Delta E}{\Delta l}$ versus range method. In particular

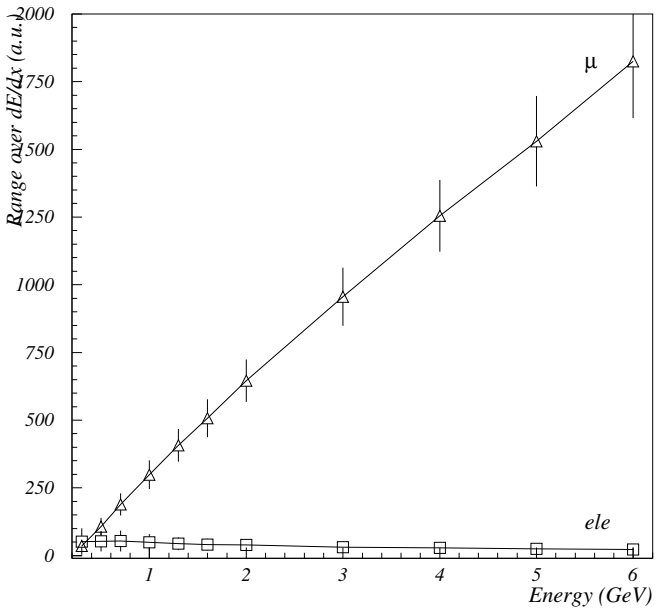

Figure 5.7: The electron - muon discrimination using $\frac{Range}{dE/dx}$ parameter.

the parameter

$$\frac{Range}{\frac{1}{n}\sum_{k=1}^{n}\left(\frac{\Delta E}{\Delta l}\right)_k}$$

can be measured for each track.

This parameter is very powerful in distinguishing between a penetrating particle, as a muon, with a long range and a poor energy released, and a showering particle, as a pion or an electron, characterized by a bigger amount of energy deposited in a shorter path. Fig. 5.7 shows this parameter, as a function of energy, for muons and electrons (for each considered energy, the mean and the standard deviation of the corresponding $\frac{Range}{\Delta E/\Delta x}$ distribution are plotted). The same parameter, as a function of energy, is used to distinguish muons from charged pions, as shown in Fig. 5.8.

Further variables can be exploited to achieve a good discrimination power, as an example the 'over-2 mip energy'$/E_{total}$ is shown in Fig. 5.9 for electrons and muons. In all cases a clear separation is evident starting from about 1 GeV of incident energy. It is important to emphasize that this result has been obtained only on the basis of the calorimetric informations. Topological informations about the energy losses distribution must be added to the

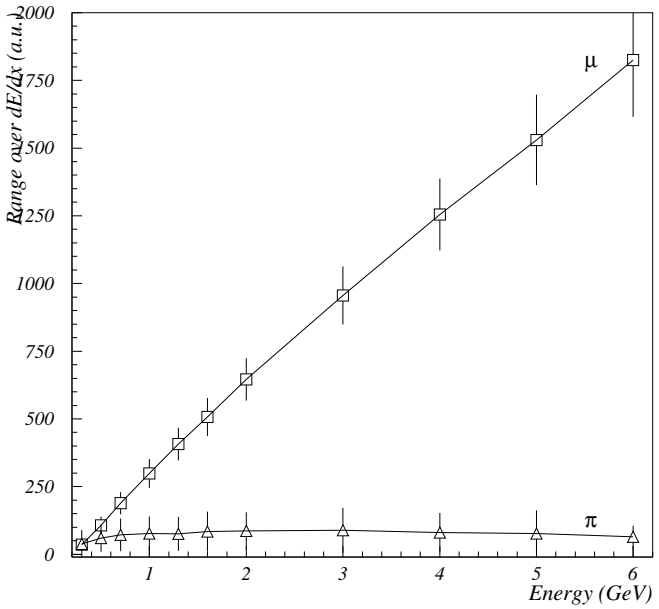

Figure 5.8: The pion - muon discrimination using $\frac{Range}{dE/dx}$ parameter.

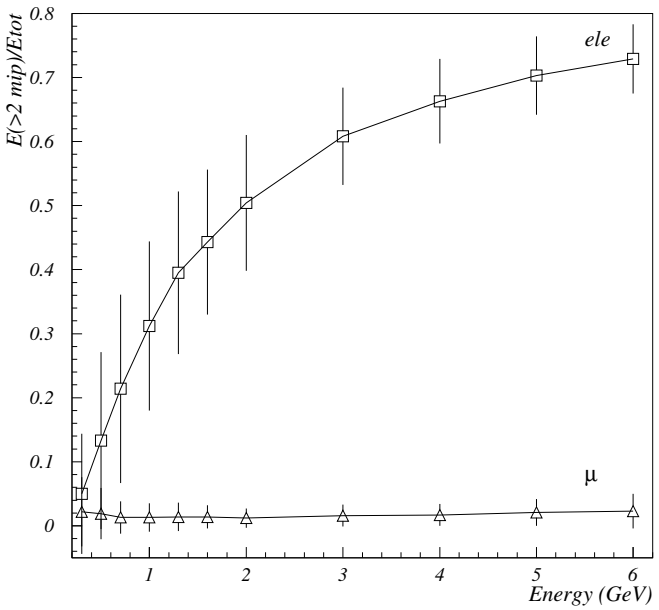

Figure 5.9: The electron - muon discrimination using $\frac{E>2\ mip}{E_{tot}}$ parameter.

calorimetric informations, in order to have discrimination between different showering particles, as electrons and pions.

Many criteria are under investigation in order to discriminate electrons from pions by exploiting differences both in the longitudinal shower development and in the lateral energy deposit.

In Fig 5.10 the shower development for electrons and hadrons, for different energies, is shown. As it is well known, the electromagnetic and hadronic showers have different development and this feature suggests to use the ratio "max. shower depth/max shower charge" as a possible discriminating parameter.

In addition, to distinguish electromagnetic and hadronic shower exploiting their different lateral profile, it is defined a quantity R that is a measure of the width of the shower:

$$R = \frac{\sum_i r_i \cdot E_i}{\sum_i E_i}$$

where E_i is the energy deposited in an individual $(BCE)_i$ and r_i is the distance between the $(BCE)_i$ and the center of gravity of the shower energy deposit.

The simulated shower transverse dimension, at the maximum of its lateral development, is shown in Fig. 5.11 for electron and pion generated cascades at different energies. For each considered energy, the mean and the standard deviation of the corresponding distribution are plotted.

Many readout solutions are under study in order to acquire all the informations necessary to the described analyses. In particular, the parameter R can be determined at the best either dividing the BCE grid read out in two transverse segment (see section 3.4.1) and then looking at the energy on a bianode PMT, or collecting the BCE's cluster hits in a finer grid readout $(3 \times 3, 4 \times 4)$ (see Fig. 3.12). For the final choice, cost and resolution have to be taken into account.

In Fig. 5.12, 5.13, 5.14, 5.15 some simulated interactions inside the calorimeter when BCE elements are upgraded by multianode PMT (or HPD) are shown. These pictures were obtained assuming that the signals produced by the 330 fibers of each BCE are collected in an multianode 4×4 PMT.

5.4 Timing features

One of the main features of the $N^{O}E$ detector is the possibility to obtain a detailed fast time information (see Fig.4.9) along all the *tracks*. The use

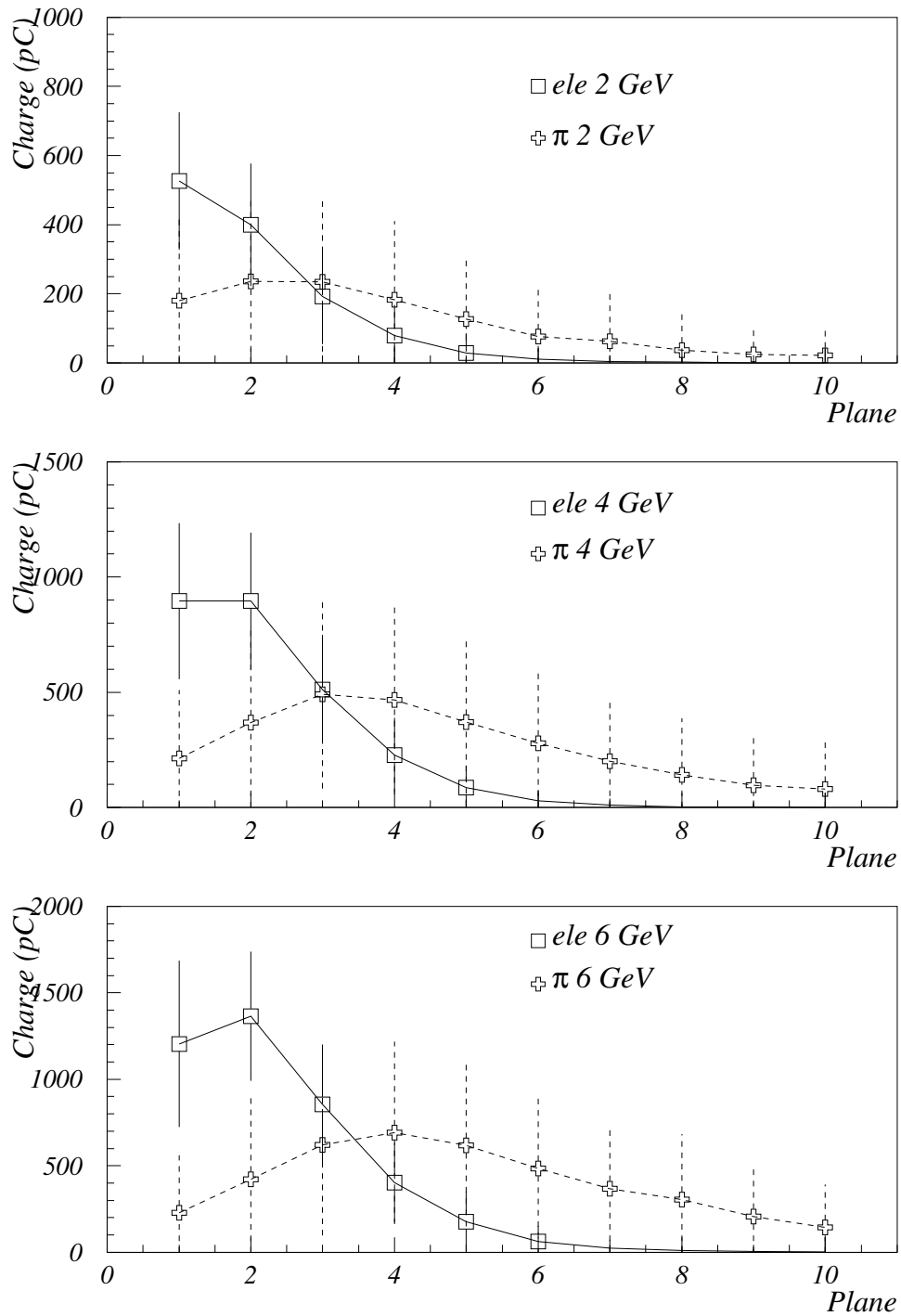

Figure 5.10: Shower development for pions and electrons (2,4,6 GeV). The mean and the standard deviation of the charge distributions are plotted.

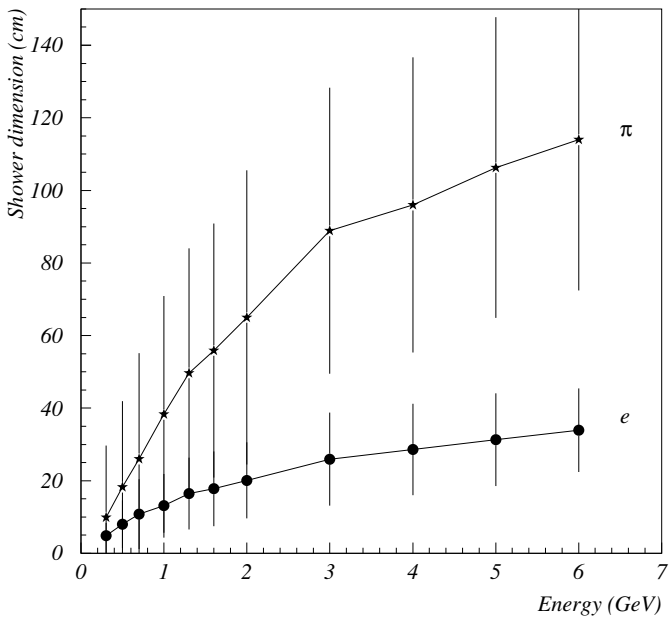

Figure 5.11: Shower maximum transverse dimension.

of this time capability improves the NOE performances in comparison with detectors that do not have so fast timing information.

In particular it is possible to have:

- low energy threshold (particularly suitable for atmospheric neutrinos)
- identification of the *direction* of the lepton produced by atmospheric neutrinos (especially useful for completely contained events).
- efficient identification of downgoing ν interacting in the apparatus, that are background for the upward stopping μ. This is relevant for the evaluation of the ratio of stopping muons/crossing muons as a figure of ν oscillation, as discussed in chapter 7.
- $\mu \to e$ decay measurement. This improves, in particular at low energy, the discrimination of contained ν_μ, ν_e CC events.
- $\pi, K \to \mu$ decay detection, which allows to discriminates delayed μ from π, K decay with respect to prompt μ from direct CC interaction.

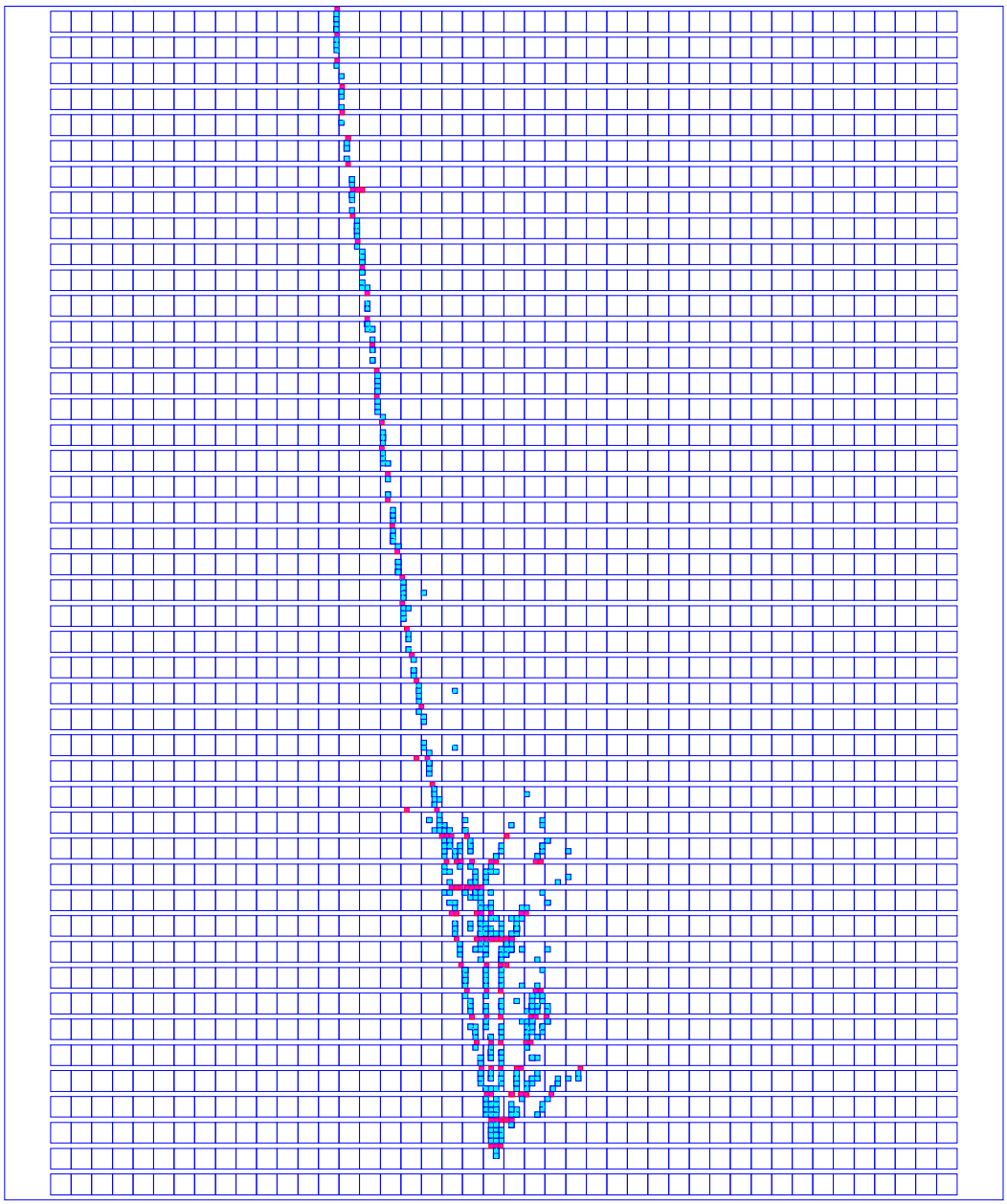

Figure 5.12: The simulated event topology with multianode readout at one side BCE: a typical charged current muon.

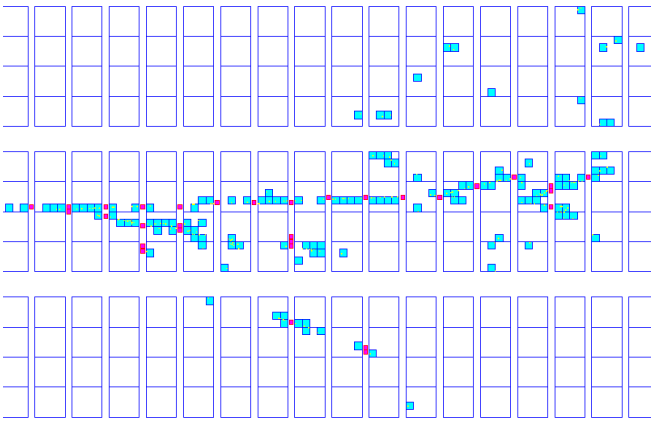

Figure 5.13: A typical 5 GeV charged pion.

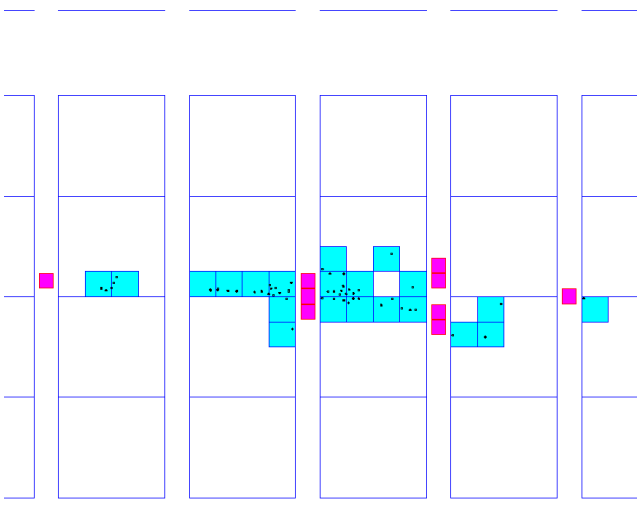

Figure 5.14: A typical 1 GeV electron.

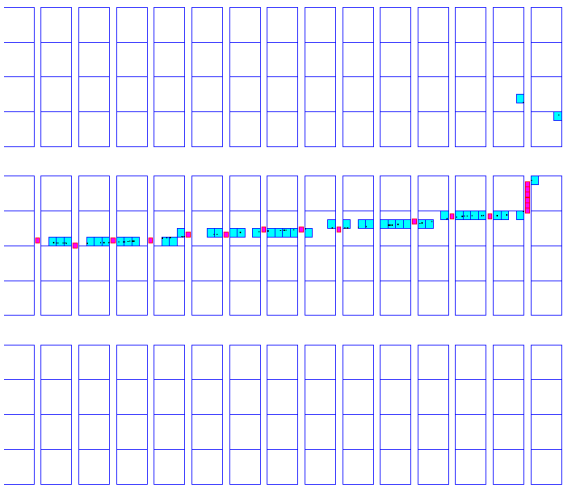

Figure 5.15: A typical 1 GeV muon; the decay electron is clearly visible.

Bibliography

[1] R.Brun et al. "GEANT - detector description and simulation tool", CERN Program Library Vers. 3.21, W5013 (1993)